Constitutive relations from images

Adeline Wihardja and Kaushik Bhattacharya

California Institute of Technology

Dedicated to Richard D. James whose work exemplifies the interplay between theory and experiment, and fidelity to both experimental observations and mathematical rigor.

Abstract

Constitutive relations close the balance laws of continuum mechanics and serve as a surrogate for a material in the design and engineering process. The problem of obtaining the constitutive relations is an indirect inverse problem where both the relation and the quantities that define the relation have to be inferred from experimental observations. The advent of full-field observation techniques promises a new ability to learn constitutive relations under realistic operational conditions. However, this is done in two steps, first obtaining deformations from the images, and then obtaining the constitutive relation from deformations and forces. This leads to a variety of difficulties. In this paper, we propose a novel approach that enables us to obtain constitutive relations directly from the raw data consisting of images and force measurements.

1 Introduction

The design of structural, aerospace, protection, and other thermomechanical engineering systems requires a constitutive relation that describes the material properties [14, 6], and is empirically determined. The essential challenge is that we cannot measure these constitutive relations directly; in fact we cannot even measure the quantities like stress, heat flux, energy density, and state variables that describe the constitutive relations.

The traditional approach relies on uniform states (e.g., uniaxial tension) or universal solutions (e.g., torsion) [6]. Each test provides limited information, and they require repetition. This has been addressed with automation and high-throughput approaches [21]. However, this is not always possible, since some experiments (e.g., plate impact) need sterile conditions with precise alignment to obtain the desired state [20]. In any case, all of these still sample idealized states of strain. These limit the fidelity of the resulting models when we use them to model complex situations. We propose to develop methods that can provide high fidelity constitutive relations by probing complex domains and complex states by using full field techniques like digital image correlation (DIC) [25, 15] and thermal imaging.

DIC takes a series of images of a decorated surface undergoing deformation and compares them to infer the deformation [25, 15]. It has emerged as a method of choice due to the ease

of using it with the widespread availability of cameras and robust commercial (e.g., [2]) and open source (e.g., [1]) software. The full-field information it provides also gives useful insight. It has been extended beyond optical imaging (e.g., [16] using scanning electron microscopy images), to digital volume correlation [9, 30], and tomography [19]. The deformation is then used to obtain constitutive relations.

This current practice of splitting the inverse problem into two inverse problems, first image to deformation, and second deformation and force to constitutive relation, poses a number of challenges. First, these inverse problems may be ill-posed and have to be regularized. When they are done separately, the regularization of one problem can limit the information available to the other problem. Indeed, DIC as a purely kinematic problem of inferring deformation is ill-posed. In practice, it is either regularized using filters or constrained by finite dimensional (local or global) ansatz. However, finite dimensional approximations do not necessarily converge, and regularization limits the efficacy when there are cracks, shear bands, and shocks. Further, we image a fixed region of space that may correspond to different parts of the body in different snapshots. So, image registration limits us to small displacements. One can stitch together multiple snapshots, but errors may be compounded, and the method is inaccessible to dynamic events where one has very few snapshots.

Second, even when a reasonable deformation is available, the second inverse problem is still a difficult problem since we cannot directly measure stress, but have to infer it from the total force acting on a part of the boundary. So it is still common to use simple configurations, though the full-field inversion is a subject of active research, and we refer the reader to [4] for a recent literature survey.

Third, we may have a mismatch of sensitivities. Even if the overall sensitivity is reasonable, the splitting into two problems leading to situations where the first inversion has low sensitivity, but the second has high sensitivity. This leads to significant errors.

Finally, there are phenomena where the instrument and the experiment are intimately coupled, rendering a sequential inversion impossible or dependent on unverifiable ansatz. For example, Lawlor *et al.* [18] recently introduced a speckle pattern in the interior of a transparent specimen and were able to observe the interaction between a shock wave and a pore. However, due to the photoelastic effect that changes the refractive index under stress, the image is heavily distorted in the vicinity of the shock as well in the wake of the shock.

In this paper, we propose an alternate approach where we study the integrated inverse problem of inferring constitutive relations directly from raw data in the form of images of speckle patterns and overall forces. We formulate this as an optimization problem and solve it using a gradient-based approach. We focus on finite elasticity and rubber, and demonstrate the method using both synthetic and experimental data.

The study of the mechanical properties of rubber goes back to seminal works of Treloar [28], Rivlin and Saunders [24], and Gent and Rivlin [12]. Assuming incompressibility, one can fully characterize the material by applying two principal stretches independently, and this motivated the biaxial tension test [24] that is widely used [3, 27]. These and other approaches [17, 5, 7] seek to create a uniform state. Others use universal solutions [11] like torsion [28] and inflation [12]. More recent efforts study complex deformations in two and three dimensions, exploiting advances in optical microscopy [23, 13, 10] and x-ray computed tomography [29]. This leads to the inverse problem that is the focus of this work.

We provide the formulation in Section 2. We demonstrate the approach using synthetic

data in Section 3, and experimental observations in Section 4. We conclude in Section 5

2 Formulation

We assume that the material is hyperelastic, and is governed by a stored energy per unit reference volume W. We assume a parametrized form, so that $W = W(F; P)$, where F is the deformation gradient and $P \in \mathbb{R}^P$ is a set of parameters. Our goal is to find the parameters from an experiment.

2.1 Image to constitutive relation

We consider a body occupying the region $\Omega \subset \mathbb{R}^n$ in the natural reference configuration. We fix part of the boundary $\partial_0 \Omega$, and apply a time dependent Dirichlet boundary condition $y(x, t) = \bar{y}(x, t)$ on another part $\partial_y \Omega$. The remainder of the boundary is traction-free. At each instant t, the body is in equilibrium, and the deformation $y : \Omega \to \mathbb{R}^n$ satisfies

$$\nabla \cdot W_F(\nabla y; P) = 0 \text{ on } \Omega \tag{1}$$

subject to the boundary conditions where $W_F = \partial W / \partial F$. Equivalently,

$$-\int_\Omega (W_F(\nabla y; P) \cdot \nabla \varphi) \, d\Omega = 0 \qquad \forall \, \varphi \in \mathcal{U} = \{u = 0 \text{ on } \partial_0 \Omega \cup \partial_y \Omega\}. \tag{2}$$

We decorate a part of the traction-free boundary of the body with a speckle (or other distinctive) pattern, and image a certain region of space $\mathcal{R}$ that contains a part of the traction-free part of the boundary to obtain images $g(y, t)$ (we typically obtain a series of snapshots). We also measure the total reaction force on the part $\partial_y \Omega$.

Our goal is to obtain P from the observations $\{g(y, t), f(t)\}$, by matching them with the corresponding quantities computed with a model with parameters P. We formulate this as an optimization problem

$$P = \arg \min \mathcal{O}(P), \tag{3}$$

where the objective is

$$\mathcal{O} = \int_0^t w(t) \left(\int_\mathcal{S} |g_0(x) - g(y(x, t), t)|^2 \, dA + \alpha \left| \int_{\partial_y \Omega} W_F(\nabla y(x, t); P) \hat{n} \, dA - f_{\exp}(t) \right|^2 \right) dt, \tag{4}$$

and $y(x, t)$ satisfies the governing equation (2), $w(t), \alpha$ are weights, and $g_0(x) = g(x, 0)$.

We solve this by gradient descent, and therefore seek to calculate the sensitivity of the objective with respect to the parameters. Doing so directly requires us to calculate y_P, the sensitivity of the solution to the governing equation (2) to the parameters; this is difficult. Therefore, we use the adjoint equation [22, 8]. To derive this equation, add the left hand

3

side of (2) to our objective, and then differentiate with respect to P. We obtain,

$$\frac{d\mathcal{O}}{dP} = \int_0^t \left(-2 \int_\mathcal{S} w(t)(g(x,0) - g(y(x,t),t))g_y y_P \, dA \right.$$
$$+ 2\alpha w(t) \left(\int_{\partial_y \Omega} W_F \hat{n} \, dA - f_{\exp}(t) \right) \cdot \left(\int_{\partial_y \Omega} (W_{FF}\nabla y_P + W_{FP}) \, \hat{n} \, dA \right) \qquad (5)$$
$$\left. + \int_\Omega (W_{FF}\nabla y_p + W_{FP}) \cdot \nabla \varphi \, dx \right) dt$$

where W_F, W_{FF}, W_{FP} are all evaluated at $(\nabla y(x,t); P)$. This still contains the problematic quantity y_P. However, this expression is true for all $\varphi \in \mathcal{U}$ (cf. (2)). We now make a special choice such that we eliminate y_P from above. Specifically, let φ satisfy the *adjoint equation*

$$\int_\Omega \nabla \psi \cdot W_{FF}\nabla \varphi \, dx + \int_\mathcal{S} \mu(x,t)\psi \, dA + \int_{\partial_y \Omega} \nabla \psi \cdot W_{FF}(\lambda(t) \otimes \hat{n}) = 0 \, dA \qquad \forall \, \psi \in \mathcal{U} \quad (6)$$

where we have used the fact that W_{FF} has major symmetry and

$$\mu(x,t) = -2w(t)(g_0(x) - g(y(x,t),t))g_y, \quad \lambda(t) = 2\alpha w(t) \left(\int_{\partial_y \Omega} W_F \hat{n} \, dA - f_{\exp}(t) \right). \quad (7)$$

Then, the sensitivity of the objective with respect to the parameter is

$$\frac{d\mathcal{O}}{dP} = \int_0^t \left(\int_\Omega W_{FP}(\nabla y(x,t); P) \cdot \nabla \varphi \, dx + \lambda(t) \cdot \int_{\partial_y \Omega} W_{FP} \, \hat{n} \, dA \right) dt. \qquad (8)$$

2.2 Numerical method

We start with an initial guess for the parameters, and then solve the forward and inverse problem using a finite element method, use the sensitivity to update the parameters, and iterate until a convergence criteria is met. Note that the forward problem is non-linear and we solve this iteratively using Newton-Raphson iteration. We discretize both the forward and the inverse problem with a 3D brick element and a standard piecewise polynomial Lagrange basis function of degree 1. The parameters are updated using method of moving asymptotes (MMA) [26] until either the norm of the sensitivities or the incremental objective reaches $\varepsilon = 10^{-5}$. Algorithm 1 summarizes our approach.

The calculation of μ requires some care. Since this term involves quantities from images that are typically pixelated, the integration is performed by locating pixels in each element and summing over these pixels (instead of quadratures). Further, the imaging is performed in the current configuration, and the current image $g(y,t)$ is in pixelated form with uniform pixel spacing in y (current configuration). However, we integrate it over the reference domain. Therefore, we have to pull it back to the reference configuration by finding the values of $g(y(x,t),t)$ where x is sampled uniformly in the reference domain. We use bilinear interpolation to do so. We compute $\nabla_y g$ by pixel differences in the current configuration and then interpolate to pull it back to the reference configuration. While this term can be noisy, it is integrated against the shape function that is smooth on the scale of the pixels, and leading to a stable calculation of μ.

4

Algorithm 1 Constitutive relations from images

Input: Reference image g_0, deformed images g, parametrized model
Output: Displacement y

    Step 1: Initiate guess of parameters P;
    Step 2: Pick region of interest ($\mathcal{S}$) to perform correlation;
    Step 3: Determine locations of each pixel in each finite element within $\mathcal{S}$;
    Step 4: Precompute spatial gradients of the image ∇g;
    while $\|d\mathcal{O}/dP\|$ **or** $\|\mathcal{O}_k - \mathcal{O}_{k-1}\| > \varepsilon$ **do**
        Step 5: Solve forward problem for displacement $y_k(x,t)$;
        for each *pixel in each finite element in $\mathcal{S}$* **do**
            Step 6: Compute $g(y(x,t),t)$, g_y from $y_k(x,t)$;
        end for
        Step 7: Solve adjoint problem for adjoint variable $\varphi_k(x,t)$;
        Step 8: Compute objective $\mathcal{O}(y_k, P_k)$;
        Step 9: Compute sensitivity $d\mathcal{O}(y_k, P_k)/dP$ for each P;
        Step 10: Update parameters $P_{k+1} = P_k + \delta P$ with MMA;
    end while

2.3 Contrast with the purely kinematic DIC

Before we demonstrate the proposed method in the next section, we comment on the mathematical issues associated with the current practice of treating digital image correlation as a purely kinematic problem of finding deformations. In this approach, we compare the image $g_0(x)$ of a decorated surface before deformation with $g(y)$ after the deformation occurs to obtain the deformation $y(x)$. Specifically, we maximize the correlation between the reference and convected images over all possible deformations, or equivalently, minimize the L^2 norm between the reference and convected images over all possible deformations,

$$y = \arg\max \int_{\mathcal{S}} g_0(x)g(y(x))\,dA = \arg\min \int_{\mathcal{S}} |g_0(x) - g(y(x))|^2\,dA. \tag{9}$$

The two formulations are equivalent since expanding the second integral gives us the first up to a factor (-2) and the L^2 norm of the images (that are independent of the deformation).

    Unfortunately, this problem is ill-posed. Note that the second problem in (9) is the classical optimal transport problem of Monge (transporting a mass with density g_0 to a mass with density g), and y is called the transport map. Unfortunately, this problem is not mathematically well-posed, and solutions may not exist and minimizing sequences may not converge. The relaxation, according to Kantorovich, is to look for minimizers over transport plans, $G(x,y)$, such that

$$\min_G \int_{\mathcal{S}} G(x,y)\,|x-y|^2\,dA \times dA \tag{10}$$

subject to

$$\int_{\mathcal{S}} G(x,y)\,dA_y = g_0(x), \quad \int_{\mathcal{S}} G(x,y)\,dA_x = g(y). \tag{11}$$

In essence, the image intensity at some reference point x can get spread over a region of

the spatial domain, and the intensity at the spatial point y may come from a region of the reference domain. In short, the solution to the classical DIC problem (9) may not exist.

In practice, we make a finite dimensional ansatz on the deformation. Two are common. The first is local, where we select a grid of points $\{\bar{x}^i\}$ and assume that the deformation is piece-wise affine in a sub-domain around these points

$$y(x) = \sum_i (y^i + F^i(x - \bar{x}^i))\chi_i(x), \tag{12}$$

where χ_i is the indicator function of the ith sub-domain around $\bar{x}^i$. The second is non-local where the deformation is given in terms of a finite-dimensional (often finite-element based) basis set $\{\psi_i\}$,

$$y(x) = \sum_i y^i \psi_i(x) \tag{13}$$

These constraints yield a solution, but there is no notion of convergence as the number of grid-points or basis functions goes to infinity. Further, this constraint to finite dimensions makes the method fail or have poor accuracy when there are cracks, shear bands, and shocks.

There are other difficulties with a purely kinematic approach. We image a fixed region of space that may correspond to different parts of the body in different snapshots. So, image registration limits us to small displacements. One can stitch together multiple snapshots, but errors can be compounded, and the method is inaccessible to dynamic events where one has very few snapshots. Further, there are situations where the deformation and imaging interact as, for example, in the recent work of Lawlor *et al.* [18] mentioned in the introduction.

Note that we overcome these difficulties in our proposed approach, since the deformation is obtained from the equilibrium equation (2) and thus is well defined.

3 Testing the idea with synthetic data

We test the idea by using synthetic data: we use a known constitutive relation, solve the forward problem with that constitutive relation, and use it to generate synthetic data. We then use the procedure described in Section 2 on the synthetic data to obtain the constitutive relation. Comparing the inferred constitutive relation with the known constitutive relation provides us with a verification of the method.

3.1 Homogeneous material

We consider a compressible hyperelastic constitutive relation motivated by neo-Hookean:

$$W = \frac{\mu}{2}\left(\text{tr}(F^T F) - 3 - 2\log(\det F)\right) + \frac{\kappa}{2}(\det F - 1)^2 \tag{14}$$

where the parameters are the shear and bulk moduli $P = \{\mu, \kappa\}$. We consider a specimen $(0, \ell) \times (0, w) \times (0, t)$ in the form of a rectangular strip with a central circular hole as shown in Figure 1(a). We create a speckle pattern $(g(x, 0))$ from correlated solutions [2] also as shown. We clamp this specimen with the constitutive relation (14) on the left $(y(\{0, x_2\})) = \{0, x_2\}$, and apply a horizontal displacement on the right $y(\{\ell, x_2\})) = \{(1 + \dot{\bar{\varepsilon}}t)\ell, x_2\}$ where the
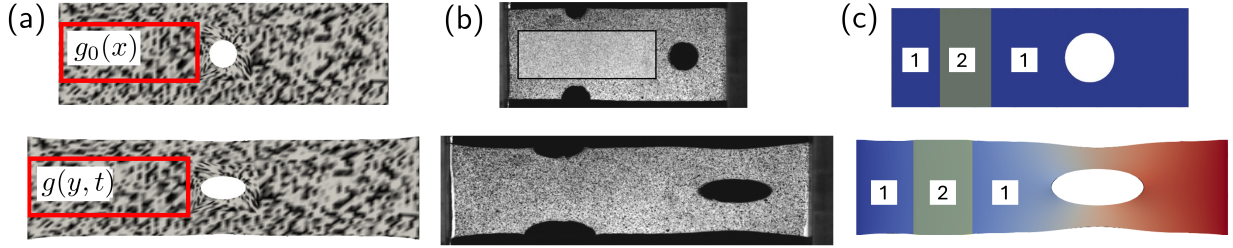
6

Figure 1: Images of reference and deformed configuration for (a) testing, (b) experimental validation, and (c) two-material example. The region of interest to perform correlation is highlighted in red in (a).

nominal strain rate $\dot{\bar{\varepsilon}}$ is taken to be extremely small. The lateral surfaces, $x_2 = 0, w$, are traction-free. We solve the equilibrium equation (2) at each time t to obtain the synthetic deformation $y(x, t)$. We obtain the speckle pattern in the current configuration by convecting the reference image by the deformation:

$$g(y, t) = g_0(x(y, t)) \tag{15}$$

where $x(y, t)$ is the inverse deformation. A snapshot is shown in Figure 1(a). We also compute the total reaction force $f(t)$ at $x_1 = \ell$ at each instance. We use $\{g_0, \dot{\bar{\varepsilon}}\}$ and a number of snapshots of $\{g, f\}$ as our data.

Known constitutive relation. We start with a situation where the constitutive relation used to generate the data is the same as assumed in the inference, and we seek to find the parameters. A typical result is shown in Figure 2. The data is generated with a initial parameters $\mu = 4\,\mathrm{MPa}, \kappa = 8.67\,\mathrm{MPa}$, and the calculation is initialized with $\mu = 8\,\mathrm{MPa}, \kappa = 7.3\,\mathrm{MPa}$. Figure 2(a) shows the reference image of the specimen with the finite element grid used for the simulations, the speckle pattern and the region of correlation $\mathcal{S}$ marked. The overall dimensions are $0.036 \times 0.012 \times 0.005$ m. Figure 2(b) shows the objective and the sensitivity, while Figure 2(c) shows the material parameter as the iteration proceeds. We observe a quick drop in the objective, a steady drop in the sensitivity, and a stable value for the parameters. The recovered values are $\mu = 3.98\,\mathrm{MPa}, \kappa = 8.58\,\mathrm{MPa}$, in close agreement with the values that generated the data.

We repeat the simulation with several values of the initial guess, and data generated with three sets of parameters. The results are shown in Table 1. We see that we obtain very good recovery in each case.

We now turn to noisy data. Images obtained from an experiment have noise depending on the experimental setup and pixel accuracy, and so we seek to test our approach against noisy data. We generate images with $720{\times}240$ pixels and $360{\times}120$ pixels within the domain and add 10% uniformly distributed random noise to the speckle values for all pixels. The range of speckle values is between 0 and 1, hence, the maximum absolute noise value is 0.1. As before, the synthetic data is generated with $\mu = 4\,\mathrm{MPa}$ and $\kappa = 8.67\,\mathrm{MPa}$. The initial
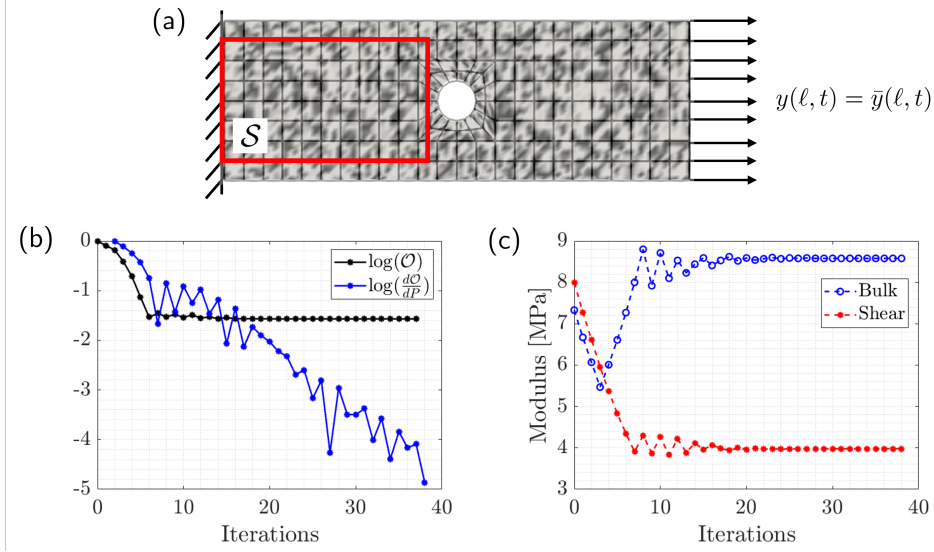
Figure 2: Results for quasistatic uniaxial tensile test of specimen shown in (a). The red box is the region to perform image correlation, $\mathcal{S}$. (b) The normalized objective in (4) and the combined sensitivity of material parameters with iterations. (c) The evolution of shear and bulk modulus. The synthetic data is generated with $\mu = 4\,\text{MPa}, \kappa = 8.6\,\text{MPa}$ and the optimization is run with initial guess of $\mu = 8\,\text{MPa}, \kappa = 7.3\,\text{MPa}$.

	Initial guess		Recovered value	
Case	Shear modulus, μ_i	Bulk modulus, κ_i	Final shear, μ_f	Final bulk, κ_f
Set 1: Generate data using $\mu = 4$ MPa, $\kappa = 8.67$ MPa				
1a	4 MPa	38 MPa	3.95 MPa	8.63 MPa
1b	1 MPa	9.67 MPa	4.03 MPa	8.35 MPa
1c	0.4 MPa	3.8 MPa	3.95 MPa	8.61 MPa
1d	40 MPa	387 MPa	3.95 MPa	8.50 MPa
1e	0.4 MPa	0.36 MPa	3.98 MPa	8.52 MPa
1f	8 MPa	7.34 MPa	3.98 MPa	8.58 MPa
1g	5 MPa	6.67 MPa	3.99 MPa	8.61 MPa
Set 2: Generate data using $\mu = 4$ MPa, $\kappa = 38.6$ MPa				
2a	1 MPa	3 MPa	3.99 MPa	33.3 MPa
2b	8 MPa	10 MPa	3.99 MPa	33.3 MPa
2c	2.2 MPa	7 MPa	4.38 MPa	36.0 MPa
Set 3: Generate data using $\mu = 0.5$ MPa, $\kappa = 4.83$ MPa				
3a	1 MPa	2 MPa	0.55 MPa	4.48 MPa
3b	0.1 MPa	0.8 MPa	0.49 MPa	4.19 MPa
3c	0.3 MPa	1.0 MPa	0.5 MPa	4.16 MPa

Table 1: Performance with various initial guesses and various sets of synthetic data.
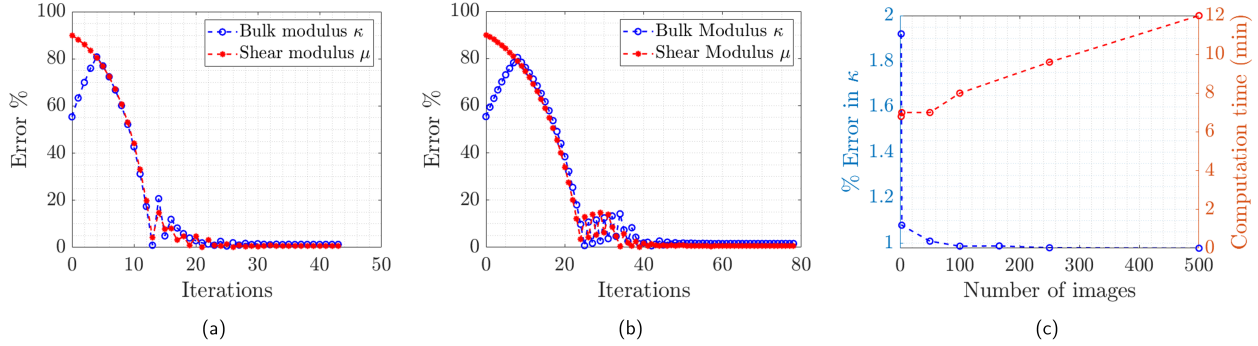
Figure 3: Performance with (a) 10% random noise in for synthetic images with 720×240 pixels and (b) 360×120 pixels. (c) Various number of images for inversion.

	Total pixels			Mesh refinement	
% Error	180×60	360×120	720×240	$1 \times$ mesh	$2 \times$ mesh
Shear modulus, μ	0.5%	0.4%	0.4%	0.8%	0.4%
Bulk modulus, κ	2.4%	1.3%	0.6%	1.5%	1.3%

Table 2: Performance tests: Errors for various image and mesh resolution.

guess of parameters is $\mu = 0.4\,\text{MPa}$ and $\kappa = 0.44\,\text{MPa}$. The evolution of material parameters can be seen in Figure 3 (a,b). We note that the method is able to recover both parameters with just 4% error.

We study the performance of our method with 2, 3, 50, 100, 250, and 500 snapshots of $g(y,t)$, resulting in errors of $1.9\%, 1.1\%, 1.0\%, 0.99\%, 0.98\%, 0.97\%$ in the bulk modulus, respectively. The error is bulk modulus and computational time per iteration can be seen in Figure 3(c). In all cases, the number of optimization iterations using MMA method is 35, 35, 37, 39, 39, and 34, respectively. Thus, we get reasonable recovery with two snapshots and this improves mildly with more snapshots.

We conclude this study by looking at a few computational issues. We study the performance of the method under refinement for both the image and the finite element discretization. In each case, the synthetic data is developed using parameters $\{\mu, \kappa\} = 4\,\text{MPa}, 8.67\,\text{MPa}$, and the simulations are initialized with parameters $\{\mu, \kappa\} = 8\,\text{MPa}, 7.34\,\text{MPa}$. Table 2 summarizes the effect of refining the image (pixel resolution) while keeping the finite element discretization fixed. We see that the errors are still small, though it degrades a little with decreasing image resolution. The effect of fixing the image resolution (at 360×120 pixels) and refining the mesh can also be seen in Table 2. We find a slight improvement in the recovery with a refined mesh.

Putting all these together, we conclude that the proposed method successfully recovers the parameters of a known constitutive relation.
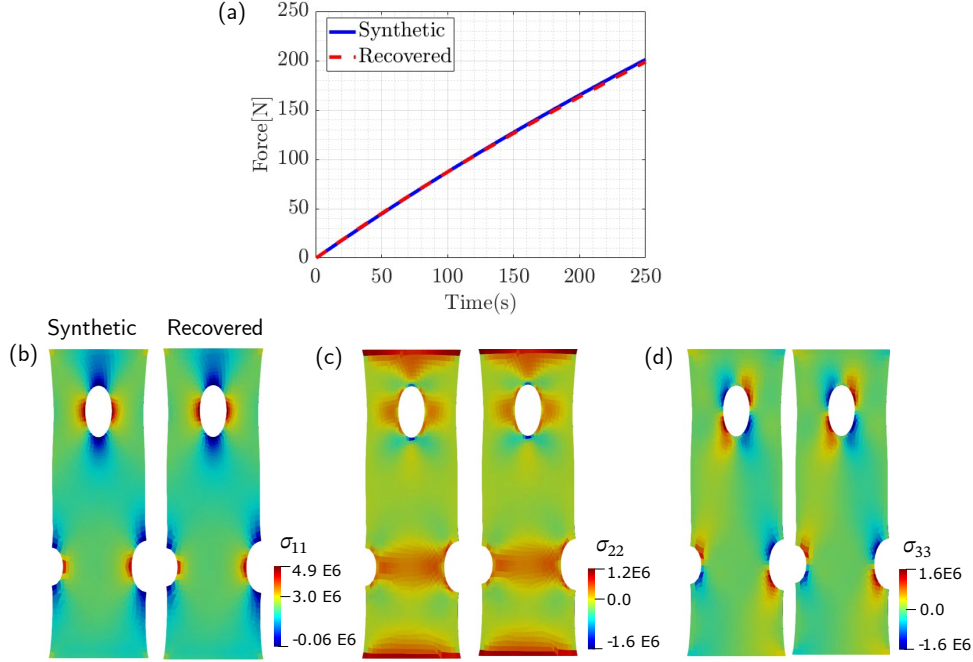
9

Figure 4: Comparison of the synthetic data and recovered constitutive relation using an independent test. (a) Force and (b-d) stress for the verification specimen at a nominal strain of 0.25.

Unknown constitutive relation. We apply our approach to synthetic data generated as described above with (14). However, in contrast to the previous example, we do not assume a knowledge of the form of the constitutive relation. Instead, we assume a different parametrized form, one motivated by a compressible Mooney-Rivlin relation

$$W = C_1(\bar{I}_1 - 3) + C_2(\bar{I}_2 - 3) + C_3(\bar{I}_1^4 - 3^4) + \kappa/2(\det F - 1)^2, \tag{16}$$

with parameters $P = \{C_1, C_2, C_3, \kappa\}$ where $\bar{I}_1, \bar{I}_2$ are the principal invariants of the left Cauchy-Green tensor, normalized by $(\det F)^{-2/3}$. We proceed as before and obtain the parameters $C_1 = 1.6$ MPa, $C_2 = 0.017$ MPa, $C_3 = 0.004$ MPa, and $\kappa = 12.4$ MPa.

To verify that the recovered constitutive relation still captures the actual constitutive behavior, we perform an independent simulation on a validation specimen with a different geometry as shown in Figure 1(b), with overall dimensions $0.05 \times 0.02 \times 0.005$ m. Figure 4(a) compares the measured and computed force between synthetic and recovered constitutive relations. Figure 4(b-d) shows the comparison of σ_{11}, σ_{22}, and σ_{22} at a nominal strain of 25%. We define the overall total error in the stress and strain fields to be

$$e_\sigma = \frac{\int_0^t \int_\Omega (\sigma_{synthetic} - \sigma_R(P))^2 \, d\Omega \, dt}{\int_0^t \int_\Omega (\sigma_{synthetic})^2 \, d\Omega \, dt}, \quad e_\epsilon = \frac{\int_0^t \int_\Omega (\epsilon_{synthetic} - \epsilon_R(P))^2 \, d\Omega \, dt}{\int_0^t \int_\Omega (\epsilon_{synthetic})^2 \, d\Omega \, dt}, \tag{17}$$

and find 0.015% error in stress and 0.014% error in strain.

Therefore, we conclude that the proposed method successfully recovers the constitutive relation even without *a priori* knowledge of the form of the constitutive relation.

10

	Initial guess		Recovered value	
Case	Shear modulus, μ_i	Bulk modulus, κ_i	Final shear, μ_f	Final bulk, κ_f
Material 1: Generate data using $\mu = 4$ MPa, $\kappa = 8.67$ MPa				
1	1 MPa	2.17 MPa	4.03 MPa	8.42 MPa
2	20 MPa	9.34 MPa	4.01 MPa	8.28 MPa
3	8 MPa	7.34 MPa	4.16 MPa	8.44 MPa
4	1 MPa	1.67 MPa	3.95 MPa	8.59 MPa
5	0.8 MPa	7.73 MPa	3.96 MPa	8.09 MPa
6	8 MPa	3.73 MPa	4.28 MPa	8.06 MPa
Material 2: Generate data using $\mu = 20$ MPa, $\kappa = 136$ MPa				
1	15 MPa	45 MPa	19.8 MPa	127 MPa
2	40 MPa	36.7 MPa	20.1 MPa	119 MPa
3	15 MPa	145 MPa	20.1 MPa	135 MPa
4	40 MPa	187 MPa	20 MPa	130 MPa
5	10 MPa	96.7 MPa	19.7 MPa	145 MPa
6	25.0 MPa	242 MPa	22.4 MPa	201 MPa

Table 3: Performance in the two-material case and various initial guesses.

3.2 Heterogeneous material

The method above can also be used when the material is piecewise uniform, as long as the domains of uniformity are identified *a priori*. The derivation of the sensitivity using the adjoint equation described earlier can easily be generalized to this case. The adjoint equation and the sensitivity are exactly as in (6) and (8) respectively, except that W depends on x. Importantly, the adjoint problem is solved only once per iteration, and the parameters for all the materials are updated simultaneously from the resulting sensitivity.

We now demonstrate the performance of our method when we have two materials as shown in Figure 1(c). We assume the constitutive law (14) for each material, but with different parameters. We generate synthetic data with $(\mu_1, \kappa_1) = (4\,\text{MPa}, 8.67\,\text{MPa})$ and $(\mu_2, \kappa_2) = (20\,\text{MPa}, 136\,\text{MPa})$ as described above. The results of our algorithm for various initial guesses are shown in Table 3. We observe excellent recovery as before.

4 Experimental demonstration

We now apply the proposed method on experimental data obtained using a natural rubber specimen (McMaster-Carr, 87145k411). We consider a specimen of size $0.036 \times 0.012 \times 0.0015$ m with a hole in the center as shown in Figure 1(a) and apply a speckle pattern of similar size to that in the figure. We clamp the left end and apply a uniaxial displacement to the right at a nominal strain rate of $\dot{\epsilon} = 0.001/$ up to a nominal strain of 45% on the Instron E3000. As the sample deforms, we record the boundary force and image the sample at 2 frames per second, with a resolution of 1024×1024 pixels of the field of view (Photron Fastcam NOVA S12 camera and Tokina AT-X PRO lens, 100F 2.8D). We use bilinear interpolation of the image to downsample the images to 720px $\times$240px.
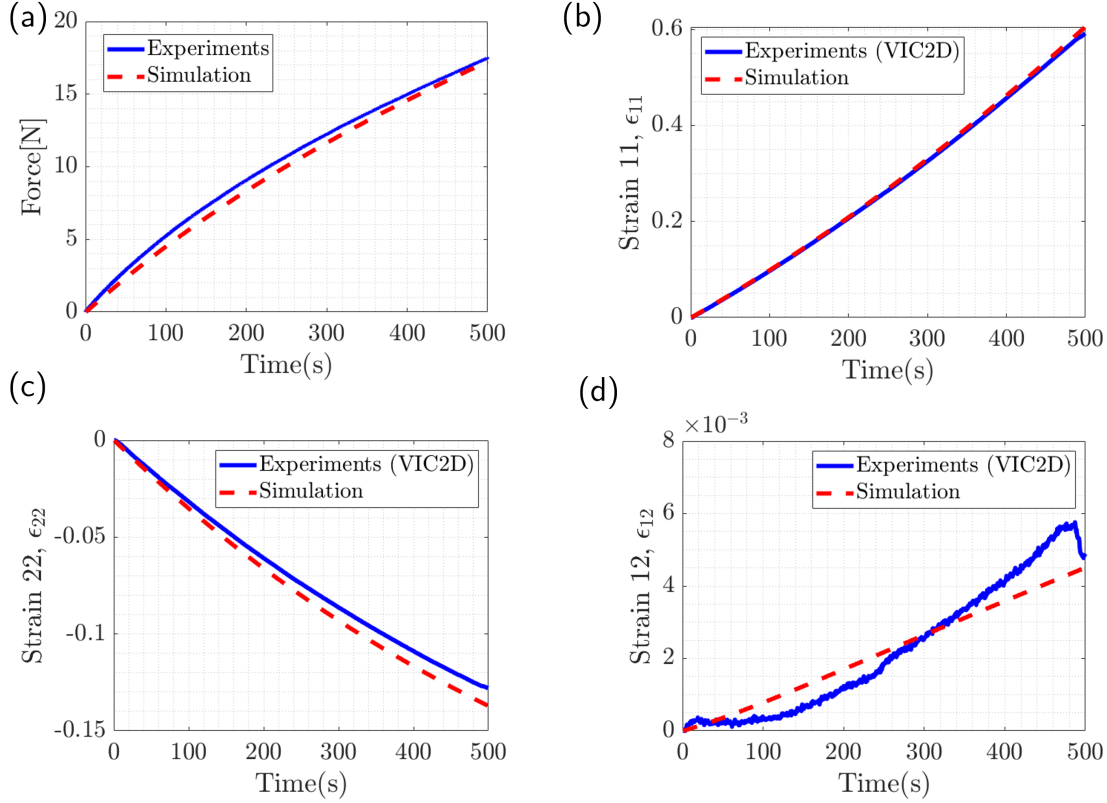
Figure 5: Comparison of the measured and computed (a) force and (b-d) average strain response for the verification specimen. The computed response uses the recovered parameters, and the strains are averaged over a region marked in Figure 1 using the recovered parameters for the verification specimen.

We then perform our method on the series of images collected. We assume that our material is described by a compressible constitutive relation motivated by the Mooney-Rivlin constitutive law,

$$W = C_1(\bar{I}_1 - 3) + C_2(\bar{I}_2 - 3) + \kappa/2(\det F - 1)^2, \tag{18}$$

with parameters $P = \{C_1, C_2, \kappa\}$ where $\bar{I}_1, \bar{I}_2$ are the principal invariants of the left Cauchy-Green tensor, normalized by $(\det F)^{-2/3}$. We obtain $C_1 = 0.33$ MPa, $C_2 = 0.21$ MPa, and $\kappa = 7.53$ MPa as the parameters from the experiment.

To verify that these recovered constitutive behavior accurately describes the material, we conduct an independent experimental test on a specimen with a different geometry shown in Figure 1(b), with overall dimensions $0.05 \times 0.02 \times 0.0015$ m. As before, the sample is deformed at $\dot{\epsilon} = 0.001/s$ up to 50% strain, and we record the force and image the specimen every 2 frames per second. Figure 5(a) compares the measured and computed force response using a finite element calculation and the recovered parameters. We find an excellent match.

We then use the recorded images and the commercial VIC2D software (Correlated Solutions, Columbia, SC) to obtain the (Lagrangian) strain field. Figure 6 compares the strain field obtained from VIC2D with that computed using finite element analysis and the recorded parameters at three loading stages. Figure 5(b-d) compares the strains averaged over a region
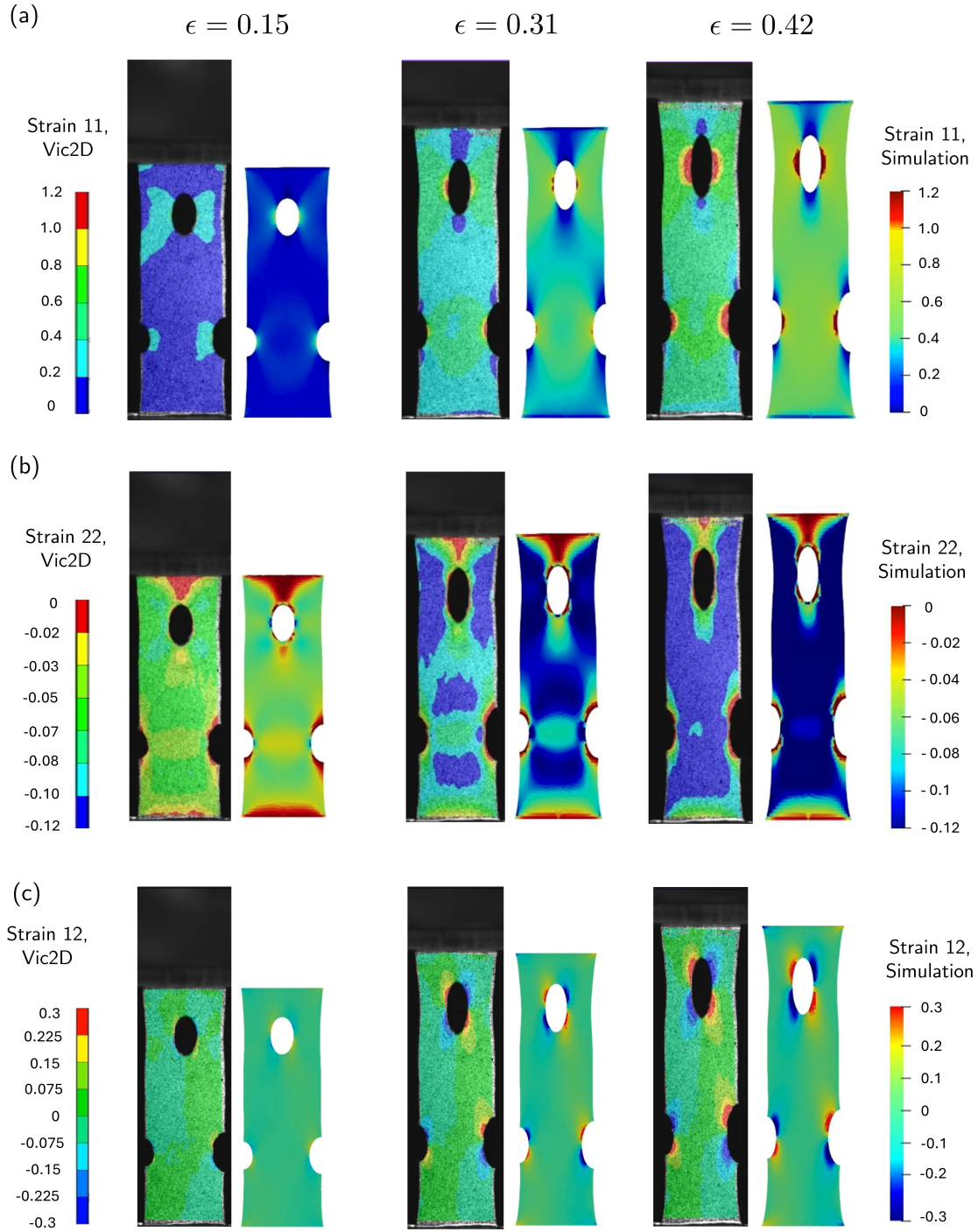
12

Figure 6: Experimental images used for verification of material parameters of a natural rubber specimen.

marked in Figure 1(b). Again, we find an excellent match. We note that the discrepancy in ϵ_{12} is comparable to the strain uncertainty of VIC-2D. The uncertainty is determined by measuring the noise floor of strain values in VIC2D by taking a series of five still images of a control sample. Under no deformation, the standard deviation of $\epsilon_{11}, \epsilon_{22}, \epsilon_{12}$ are 0.0006, 0.0005, and 0.0004 respectively.

We conclude that the proposed method successfully recovers the constitutive relation from an experimental test.

5   Conclusion

We address the problem of learning constitutive relations of materials from experiments. We seek to use the power of full-field observation techniques like digital image correlation. In a departure from previous work that breaks down the inverse problem into two nested optimization problems, first obtaining deformation from images and second obtaining constitutive relations from deformation and force, we propose an integrated approach. Specifically, we formulate the problem of obtaining constitutive relations from raw data (images and force) as a partial differential equation constrained optimization problem, and solve it using the adjoint method. The integrated approach overcomes many of the problems associated with treating digital image correlation as a purely kinematic problem of obtaining deformation from images, as well as the problems associated with a multi-level optimization. We demonstrate this approach on finite elasticity using both synthetic and experimental data. We view this as a first step in a larger program, and plan to address history-dependent behavior, shocks, fracture, and other phenomena in future work.

Acknowledgement

References

[1] ALDIC. https://github.com/jyang526843/2DALDIC.

[2] VIC2D. https://www.correlatedsolutions.com.

[3] R. Abeyaratne, C. Chu, and R. D. James. Kinetics of materials with wiggly energies: Theory and application to the evolution of twinning microstructures in a Cu-Al-Ni shape memory alloy. *Philosophical Magazine A*, 73:457–498, 1996.

[4] A. Akerson, A. Rajan, and K. Bhattacharya. Learning constitutive relations from experiments: 1. PDE constrained optimization. *Journal of the Mechanics and Physics of Solids*, 201:106128, 2025. Preprint: arXiv:2412.02864.

[5] G. Becker. On the phenomenological description of the nonlinear deformation behavior of rubberlike high polymers. *Journal of Polymer Science Part C: Polymer Symposia*, 16:2893–2903, 1967.

[6] E. Billington and A. Tate. *Physics of Deformation and Flow: An Introduction*. McGraw Hill, 1981.

[7] P. Blatz and W. Ko. Application of finite elastic theory to the deformation of rubbery materials. *Transactions of the Society of Rheology*, 6:223–251, 1962.

[8] M. Bonnet and A. Constantinescu. Inverse problems in elasticity. *Inverse Problems*, 21:R1–R50, 2005.

[9] A. Buljac, C. Jailin, A. Mendoza, J. Neggers, T. Taillandier-Thomas, A. Bouterf, B. Smaniotto, F. Hild, and S. Roux. Digital Volume Correlation: Review of Progress and Challenges. *Experimental Mechanics*, 58:661–708, 2018.

[10] J. De Crevoisier, G. Besnard, Y. Merckel, H. Zhang, F. Vion-Loisel, J. Caillard, D. Berghezan, C. Creton, J. Diani, M. Brieu, et al. Volume changes in a filled elastomer studied via digital image correlation. *Polymer Testing*, 31:663–670, 2012.

[11] J. L. Ericksen. Deformations Possible in Every Isotropic, Incompressible, Perfectly Elastic Body. *Zeit. Ange. Math. Phys.*, 5:466–489, 1954.

[12] A. Gent and R. Rivlin. Experiments on the mechanics of rubber ii: the torsion, inflation and extension of a tube. *Proceedings of the Physical Society. Section B*, 65:487–501, 1952.

[13] F. Grytten, H. Daiyan, M. Polanco-Loria, and S. Dumoulin. Use of digital image correlation to measure large-strain tensile properties of ductile thermoplastics. *Polymer Testing*, 28:653–660, 2009.

[14] M. Gurtin. *Introduction to Continuum Mechanics*. Academic Press, 1970.

[15] F. Hild and S. Roux. Digital image correlation: from displacement measurement to identification of elastic properties: A review. *Strain*, 42:69–80, 2006.

[16] A. D. Kammers and S. Daly. Digital Image Correlation under Scanning Electron Microscopy: Methodology and Validation. *Experimental Mechanics*, 53:1743–1761, 2013.

[17] S. Kawabata, M. Matsuda, K. Tei, and H. Kawai. Experimental survey of the strain energy density function of isoprene rubber vulcanizate. *Macromolecules*, 14:154–162, 1981.

[18] B. P. Lawlor, V. Gandhi, and G. Ravichandran. Full-field quantitative visualization of shock-driven pore collapse and failure modes in PMMA. *Journal of Applied Physics*, 136:225901, 2024.

[19] M. Mehdikhani, C. Breite, Y. Swolfs, M. Wevers, S. V. Lomov, and L. Gorbatikh. Combining digital image correlation with X-ray computed tomography for characterization of fiber orientation in unidirectional composites. *Composites Part A: Applied Science and Manufacturing*, 142:106234, 2021.

[20] M. Meyers. *Dynamic Behavior of Materials*. John Wiley & Sons, Ltd, 1994.

[21] D. Miracle and D. Thoma. Autonomous research and development of structural materials - An introduction and vision. *Current Opinion in Solid State and Materials Science*, 33:101188, 2024.

[22] A. A. Oberai, N. H. Gokhale, and G. R. Feijâo. Solution of inverse problems in elasticity imaging using the adjoint method. *Inverse Problems*, 19:297–313, 2003.

[23] E. Parsons, M. Boyce, and D. Parks. An experimental investigation of the large-strain tensile behavior of neat and rubber-toughened polycarbonate. *Polymer*, 45:2665–2684, 2004.

[24] R. S. Rivlin and D. Saunders. Large elastic deformations of isotropic materials vii. experiments on the deformation of rubber. *Philosophical Transactions of the Royal Society of London. Series A, Mathematical and Physical Sciences*, 243:251–288, 1951.

[25] M. A. Sutton, J. J. Orteu, and H. Schreier. *Image correlation for shape, motion and deformation measurements: Basic concepts, theory and applications*. Springer Science & Business Media, 2009.

[26] K. Svanberg. The method of moving asymptotes - A new method for structural optimization. *International Journal for Numerical Methods in Engineering.*, 24:359–373, 1987.

[27] H. Tokumoto, H. Zhou, A. Takebe, K. Kamitani, K. Kojio, A. Takahara, K. Bhattacharya, and K. Urayama. Probing the in-plane liquid-like behavior of liquid crystal elastomers. *Science Advances*, 7:abe949, 2021.

[28] L. R. Treloar. Stress-strain data for vulcanized rubber under various types of deformation. *Rubber Chemistry and Technology*, 17:813–825, 1944.

[29] Z. Wang, S. Das, A. Joshi, A. J. D. Shaikeea, and V. S. Deshpande. 3d observations provide striking findings in rubber elasticity. *Proceedings of the National Academy of Sciences*, 121(24):e2404205121, 2024.

[30] J. Yang, L. Hazlett, A. Landauer, and C. Franck. Augmented Lagrangian Digital Volume Correlation (ALDVC). *Experimental Mechanics*, 60:1205–1223, 2020.